A Search for Larson-Type Relations in Numerical Simulations of the ISM. Evidence for Non-Constant Column Densities

Enrique Vázquez-Semadeni, Javier Ballesteros-Paredes and Luis F. Rodríguez

e-mail: `enro,javier,luisfr@astroscu.unam.mx`

Instituto de Astronomía, UNAM, Apdo. Postal 70-264, México, D. F. 04510, México

ABSTRACT

We present results from a statistical study of clouds in two-dimensional numerical simulations of the interstellar medium. Clouds are defined as connected sets of pixels above an arbitrary density threshold. Similarly to real interstellar clouds, the clouds in the simulations exhibit a differential mass spectrum $dN(M)/dM \sim M^{-1.44\pm.1}$ and a velocity dispersion-size relation $\Delta v \sim R^{0.41\pm.08}$, although the latter with correlation coefficients of only ~ 0.6. However, the clouds do *not* exhibit a clear density-size relation. At a given mean density, clouds span a range of sizes from the smallest resolved scales up to a maximum given by a Larson-type relation $R_{\max} \sim \rho^{\alpha}$, with $\alpha = -0.81 \pm .15$, although numerical effects cannot be ruled out as responsible for the latter correlation. The continuum of sizes at a given mean density implies a range of column densities of up to two orders of magnitude.

This result supports the suggestion by Scalo that the observed relation may be an artifact of the observational limitations. In this case, the non-existence of a density-size relation would suggest that the origin of the Δv–R relation is not virial equilibrium of clouds that follow a $\rho \propto R^{-1}$ law. Instead, the Δv–R relation can be interpreted as a direct consequence of a k^{-2} turbulent spectrum, which is characteristic of a field of shocks, verified in the simulations. However, we also discuss the possibility that the clouds are in balance between self-gravity and turbulence, but with a scatter of at least a factor of 10 in the velocity dispersion-size relation, and a scatter of over a factor of 100 in the density-size relation, according to the equilibrium relation $\Delta v \sim (NR)^{1/2}$. In this case, the scatter in column density would be larger than the dynamic range of the simulations (and most observational studies).

Finally, we compare these results with recent observational data. We propose a simple model suggesting that recent results in which nearly constant column densities are derived for dark IRAS clouds may be an artifact of a temperature gradient within the clouds induced by external radiative heating. As a consequence, we emphasize that IRAS surface brightness maps are not appropriate for measuring column densities.

Subject headings: hydrodynamics — ISM: clouds — ISM: structure — turbulence

1. Introduction

Interstellar clouds appear to follow a set of scaling relations first noticed by Larson (1981), and then apparently confirmed (with slight modifications) by a number of other workers. These "Larson's relations" have the form

$$\rho \sim R^{\alpha} \tag{1a}$$

$$\Delta v \sim R^{\beta}, \tag{1b}$$

where R is the cloud size, ρ is the gas density, Δv is the velocity dispersion derived from the line widths, and α and β are the constant scaling exponents. Additionally, the clouds are found to exhibit a mass distribution of the form

$$\frac{dN(M)}{dM} \sim M^{n}. \tag{2}$$

The most commonly quoted values of the exponents are $\alpha \sim -1.15 \pm .15$, $\beta \sim 0.4 \pm .1$, and $n \sim -1.55 \pm .15$ (Larson 1981; Torrelles et al. 1983; Dame et al. 1986; Falgarone & Pérault 1987; Myers & Goodman 1988; Falgarone, Puget & Pérault 1992, hereafter FPP; Fuller & Myers 1992; Miesch & Bally 1994; Wood, Myers & Daugherty 1994, hereafter WMD; Caselli & Myers 1995; see also the reviews by Scalo (1985, 1987) and Blitz (1991)). However, significantly discrepant values have also been reported (e.g., Carr 1987; Loren 1989), and the validity of these scaling relations is currently the subject of strong controversy within the community.

The above "standard" values of the exponents for eqs. (1a) and (1b) have been interpreted in terms of the virial theorem (e.g., Larson 1981; Myers & Goodman 1988; Caselli & Myers 1995). For $\alpha = -1$ (which coincidentally implies constant column density), a value $\beta = 0.5$ implies virial balance between self-gravity and the internal velocity dispersion. However, note that for an arbitrary value of the density scaling exponent α, a corresponding virial balance value of β can always be found (Vázquez-Semadeni & Gazol 1995). Thus, the density-size relation (1a) remains unexplained. In fact, it has been proposed by Scalo (1990) that this relation may be a mere artifact of the dynamic range limitations of the observations, and does not reflect a real property of interstellar clouds. In particular, in the case of molecular line data, the observations are restricted to column densities large enough that the tracer molecule is shielded against photo-dissociating radiation. On the other hand, while the proportionality between line integrated CO intensity and mass surface density has been reliably established for extragalactic observations (Dickman, Snell, & Schloerb 1986), this relationship is only valid for scales at which calibrations have been possible, i.e., scales larger than a few pc. Furthermore, for clumps within molecular clouds, the structures identified in CO often do not correspond to those identified with higher-density tracers (e.g., Massi & Lizano 1994; J. Scalo, private communication).

In this paper we present the mass spectrum of clouds and search for Larson-type correlations in three two-dimensional numerical simulations of turbulence in the interstellar medium (ISM), one from Passot, Vázquez-Semadeni & Pouquet (1995, hereafter Paper I), and the other two being variants of the former with respectively larger density contrasts and larger resolution. We have developed a cloud-identifying algorithm which allows us to measure the average density, velocity dispersion and total mass within well-defined (though arbitrary) cloud boundaries in the density fields of the simulations. The cloud sample thus obtained has the advantage over actual observations that no tracer limitations exist in "detecting" the clouds, although, on the other hand, a form of saturation is present due to the relatively small density dynamic range and other numerical limitations of the simulations.

In § 2 we briefly describe the simulations and the cloud-identifying algorithm, and in § 3 we present the resulting statistical cloud properties. In § 4 we analyze the limitations of the simulations, discuss the implications of the absence of a density-size relation, and give a preliminary discussion of the physical mechanisms behind the velocity dispersion-size relation. We also compare the results with recent corresponding observations, in particular those of WMD. Finally, § 5 summarizes the results.

2. Numerical Method

Paper I presented magneto-hydrodynamical simulations of the ISM incorporating model terms for cooling, diffuse heating and local heating from star formation. The simulations solve the equations for the evolution of the density, velocity, internal energy and magnetic fields in the presence of self-gravity, namely

$$\frac{\partial \rho}{\partial t} + \nabla \cdot (\rho \mathbf{u}) = \mu \nabla^{2} \rho, \tag{3}$$

$$\frac{\partial \mathbf{u}}{\partial t} + \mathbf{u} \cdot \nabla \mathbf{u} = -\frac{\nabla P}{\rho} - \nu_8 \nabla^8 \mathbf{u} - \left(\frac{J}{M_a}\right)^2 \nabla \phi$$
$$+ \frac{1}{\rho} (\nabla \times \mathbf{B}) \times \mathbf{B} - 2\Omega \times \mathbf{u}, \quad (4)$$

$$\frac{\partial e}{\partial t} + \mathbf{u} \cdot \nabla e = -(\gamma - 1)e\nabla \cdot \mathbf{u} + \kappa_T \frac{\nabla^2 e}{\rho} + \Gamma_d + \Gamma_s - \rho\Lambda, \quad (5)$$

$$\frac{\partial \mathbf{B}}{\partial t} = \nabla \times (\mathbf{u} \times \mathbf{B}) - \nu_8 \nabla^8 \mathbf{B}, \quad (6)$$

$$\nabla^2 \phi = \rho - 1. \quad (7)$$

We refer the reader to Vázquez-Semadeni, Passot & Pouquet (1995a) and Paper I for full details on the simulations. Here we just point out that the simulations from which the data are extracted represent a square section of the ISM along the Galactic plane of size 1 kpc on a side, with a resolution of 512 grid points per dimension. Also, it is important to note that all the evolution equations contain dissipative or diffusive terms which are necessary since the numerical technique used to solve the equations (spectral method) does not produce numerical viscosity, so the dissipation must be included explicitly. The momentum and magnetic field equations contain "hyperviscosity" terms of the form ∇^8, which confine the viscous effects to the very smallest scales in the simulations (Babiano et al. 1987; McWilliams 1984). However, although globally dissipative, hyperviscosity is not everywhere positive definite (Passot & Pouquet 1988), so standard Laplacian terms are used in the continuity and internal energy equations.

Throughout the paper, densities are expressed in units of 1 cm^{-3} and velocities in units of 11.7 km s^{-1}, the units used in Paper I. In particular, in the present paper we will use data from the run labeled Run 28 in Paper I. However, the star-formation scheme used in the simulations of Paper I assumes that a star is formed wherever the local density exceeds a critical value ρ_c. (A "star" in the simulations is a point source of heat.) This naturally imposes an upper limit on the densities reached by the model, since the stellar heating increases the local pressure and causes the gas to expand. Thus, densities above ρ_c are very rarely reached. In Run 28, $\rho_c = 30$, limiting the density contrast ρ_{max}/ρ_{min} to values ~ 1000. In order to obtain a somewhat larger dynamic range, we have performed an additional run, called Run 28bis, which is identical to Run 28 up to $t = 6.5 \times 10^7$ yr, but afterwards has the star formation turned off. This run ends up collapsing gravitationally at $t \sim 8.8 \times 10^7$ yr due to the lack of support from stellar energy injection, but intermediate times provide a good framework for study, exhibiting density maxima $\gtrsim 100$ cm^{-3}, and density contrasts $\gtrsim 5000$. Finally, a run similar to Run 28bis but at a larger resolution (800×800, refered to as Run 28.800) was also performed to discuss the effects of dissipation. As an illustration, fig. 1 shows a contour plot of the density field of Run 28 at $t = 6.6 \times 10^7$ yr, with the velocity field represented by the arrows. Note that, although the size scales represented by the runs are larger than those studied by most papers concerned with cloud statistics, we expect the results to be applicable, since all terms in the equations solved in the simulations are scale-free, except for the dissipative ones.

In order to investigate the statistical properties of the clouds in the simulations, we have developed an automated algorithm which identifies and labels clouds. We define clouds as connected sets of pixels with densities above a user-defined density threshold ρ_t. The types of clouds that are identified in this way are thus clearly dependent on the value chosen for ρ_t, a somewhat similar situation to performing observations using various density tracers. As an example, figs. 2a and 2b show the clouds obtained by respectively setting $\rho_t = 4$ and $\rho_t = 16$, at time $t = 6.6 \times 10^7$ yr into the evolution of Run 28.

The extremely irregular shapes of most clouds are noteworthy, and in fact pose a problem in defining the "size" R of a given cloud. For simplicity, here we take the size of a cloud as the square root of the number of pixels it contains. This definition may be somewhat unrealistic if clouds are fractal in such a way that their perimeters are not proportional to the square root of their areas (e.g., Scalo 1990; Falgarone, Phillips & Walker 1991), but for simplicity and similarity to observational work we adopt it here. Also, for convenience, sizes are expressed in pixels in most of the figures below (1 pixel ~ 2 pc).

For each cloud found by the algorithm, it is then a trivial matter to compute the average density, the mass, and the turbulent velocity dispersion, calculated as $\Delta v \equiv \langle (\mathbf{u} - \langle \mathbf{u} \rangle)^2 \rangle^{1/2}$, where $\mathbf{u}$ is the local value of the velocity and $\langle \mathbf{u} \rangle$ is the average over the cloud area. Note that this quantity is not density-weighted.

3. Statistical Cloud Properties

We have obtained relatively large samples of clouds by considering values of ρ_t =3, 4, 6, 8, 11, 16, 23, and 29 in Run 28, and ρ_t =3, 4, 6, 8, 11, 16, 23, 32, 45, 64, and 90 in Run 28bis. Clouds obtained with each value of ρ_t are indicated with a particular symbol type in the plots discussed below. In what follows, the data from Run 28 will be considered at $t = 6.6 \times 10^7$ yr, and Run 28bis at $t = 7.15 \times 10^7$ yr, unless otherwise noted. The cloud samples for those cases contain 158 and 145 clouds, respectively.

Figures 3a and 3b show the logarithmic mass distributions of the clouds for Run28 and Run 28bis, respectively. The masses are expressed in the nondimensional units of the simulations, in which the total mass contained is $4\pi^2$, corresponding to $0.36 \times 10^7 M_\odot$ in real units. The turnover at low masses may be attributed to incompleteness due to the finite resolution. The high-mass sides of the distributions, however, exhibit least-squares slopes (fitted for $\log M > 0.8$ and shown as the straight lines) which imply indices $n = -1.51$ and -1.43, respectively (c.f. eq. [2]). These values are within the range of values reported in various observational results (e.g., WMD; see also the reviews by Scalo 1985, Blitz 1991, Mundy 1994, and references therein).

Figures 4a and 4b show the correlation between velocity dispersion and size for all clouds with sizes $\gtrsim 2$ pixels (1-pixel clouds are excluded as they have no velocity dispersion). Least squares fits to the data give slopes (shown as the solid lines) $\beta \sim 0.37$ and $\beta \sim 0.39$ respectively for Run 28 and Run 28bis, with moderately tight correlation coefficients ~ 0.6. The large scatter of about one order of magnitude in the correlations should be emphasized. This is comparable to the scatter found for molecular-line data (e.g., FPP). The derived values of $\beta \sim 0.4$ are slightly lower than the most commonly accepted value of 0.5 (dotted lines), but are remarkably close to determinations that include heterogeneous data sets (Larson 1981; FPP; Fuller & Myers 1992).

Figures 5a and 5b show the average density $\langle \rho \rangle$ vs. size for the snapshots of the two runs. Several points should be remarked. First, note that, in general, the average density of the clouds is quite similar to the value of ρ_t used to define the cloud, and in fact tends to increase with size at each ρ_t. This is not surprising, due to the presence of dense "cores" inside the largest clouds at each ρ_t, which tend to increase their average

density. Second, no clear correlation can be seen in either figure. Instead, at a given ρ_t, clouds down to the smallest possible size are seen. These are small clouds with low densities and, therefore, low column densities[1] $N = \rho R$. Third, the size of the largest cloud at each ρ_t is smaller for larger ρ_t. In particular, in both figures the set of largest clouds at each ρ_t seems to lie near a $\rho \sim R^{-1}$ law, similar to the standard exponent in Larson's relation (1a).

In order to test the robustness of the above results, we performed the same analysis at various other times in both runs, namely at t =7.8, 9.1, 10.4, 11.7 and 13.0×10^7 yr in Run 28, and t =7.8 and 8.6×10^7 yr in Run 28bis. The average value of the exponent β of the velocity dispersion-size relation is $\langle \beta \rangle = 0.41 \pm .08$, with typical correlation coefficients ~ 0.6. For the mass spectrum, an average exponent $\langle n \rangle = -1.44 \pm .1$ is found. The errors are the standard deviations of the set of values found for all times. These results confirm the fact that the simulations show correlations consistent with the observations in both cases.

Regarding the density, in all cases small clouds with low densities exist, the plots (not shown) being qualitatively similar to figs. 5a and 5b, and the full ensemble of clouds not exhibiting any correlation with size. The largest clouds at each ρ_t, on the other hand, continue to exhibit a near power-law relation with size, with average exponent $\langle \alpha \rangle = -0.81 \pm .16$. This is smaller than the slopes found in figs. 5a and 5b, which coincidentally seem to have some of the steepest slopes in the distribution. This is illustrated in fig. 6, which shows density vs. size for the largest cloud at each value of ρ_t at all times considered above for the two runs. In this figure, clouds obtained with a given value of ρ_t at any one time in either run are shown with the same symbol and joined by a dotted line. The resulting curves have been displaced by increments of 0.2 in $\log \langle \rho \rangle$ for clarity. For reference, the solid line shows a $\langle \rho \rangle \propto R^{-1}$ power law. The three uppermost curves in the figure correspond to Run 28bis and, because of the larger density dynamic range of this run, exhibit power-law behavior over a larger range of scales, while those for Run 28 saturate

---

[1]Note that the column density defined here refers to a cut through the clouds on the plane of the simulations, and has units of cm^{-2}. To obtain a column density with units cm^{-1}, appropriate to our two-dimensional problem, a multiplication by the unit length along the third (z) dimension, perpendicular to the plane of the simulation, should be performed. For simplicity, we omit this constant factor throughout the paper. A similar situation applies to the computation of masses.

at $\rho \sim 30$. For this reason, only clouds with $\log R > 1$ for Run 28bis, and with $\log R > 1.5$ for Run 28 were considered in computing $\langle \alpha \rangle$. The implications of these results are discussed in 4.2.1 For convenience, in what follows we drop the brackets when referring to the average density of clouds.

Finally, it should be pointed out that, although clouds with low column densities exist in the simulations, most of the mass still resides in the largest clouds, since the distribution of cloud sizes at a given mean density appears to be roughly uniform. However, this is possibly an effect of the absence of supernovae in the simulations, since the "expanding HII regions" included do not have enough power to disrupt the largest gravitationally bound complexes.

4. Discussion

4.1. Applicability and limitations of the results

The results presented in § 3 have important implications, provided that the simulations are indeed representative of ISM dynamics. That this is likely to be the case, in spite of their two-dimensionality, is suggested by the fact that the simulated ISM reproduces both the velocity dispersion-size relation and the mass spectrum of the clouds (c.f. § 3), as well as other physical properties of the ISM, such as the mean density of giant cloud complexes (Vázquez-Semadeni et al. 1995a), the cloud and intercloud magnetic field strengths (Paper I), the rate of formation of massive stars (Vázquez-Semadeni, Passot & Pouquet 1995b), etc. However, one important possible criticism due to the two-dimensionality, is that a $\rho \sim R^{-1}$ scaling relation in three dimensions might translate into a $\rho \sim R^0$ relation in two dimensions, just because of the elimination of one dimension. This could be at the origin of the near constancy of $\langle \rho \rangle$ observed at every value of ρ_t. Closer examination shows that this argument is invalid. Even though the clouds seem to have nearly constant densities at each value of ρ_t, this only reflects the fact that, due to our cloud-identifying algorithm, small, dense clouds are not seen at small ρ_t, since they are "hidden" within the larger, low density ones. But obviously the density is not constant in the simulations, invalidating the possibility of an R^0 dependence of the density.

Another important source of concern is that a significant fraction of the clouds in the samples have sizes of only a few pixels, and their properties are thus likely to be affected by viscosity and diffusion. Thus, it is important to quantify the extent to which the results of the previous section might be influenced by these terms. In particular, the question arises as to whether the existence of low-column density, small clouds might be an artifact of the dissipative terms.

Concerning viscosity, owing to the hyperviscosity scheme with a ∇^8 operator, its effects on the velocity field are confined to wavenumbers k in the range $k_{max}/2 \lesssim k \leq k_{max}$ with $k_{max} = 255$ for Runs 28 and 28bis, as can be seen from the spectrum in fig. 10 (see §4.2.2). The same applies to the dissipative term in the magnetic equation (see fig. 5 of Paper I). Naively, one would then expect the effects of viscosity to be present at scales up to twice the smallest scale of the simulation, i.e., from one to two pixels. Actually, the correspondence between scale ranges in real and Fourier spaces is not as sharp, and one can expect "leakage" up to possibly 4 pixels. Visual inspection of the velocity field confirms that shocks are spread over typically 4 pixels. Nevertheless, note that viscosity is not effective if the velocity gradients are not large, and thus the 4-pixel estimate is an upper limit to the sizes affected by viscosity. It is worth pointing out that in Paper I the range of influence of viscosity was estimated at ~ 5 pixels. However, this was an over-conservative estimate not based on a detailed analysis of shock widths, and the 4-pixel figure given here should be considered as a slightly more precise estimate based on the above considerations.

In order to correct for viscosity effects, clouds with sizes up to 4 pixels in size are excluded from the "corrected" plots shown in the Appendix. Note that, since clouds have in general elongated shapes and sizes are computed as the square root of the number of pixels, the possibility exists that clouds with computed sizes larger than 4 pixels will still be 4 pixels or less across one particular direction. However, we believe this effect may be roughly compensated by the fact that the 4-pixel estimate is an upper limit, and thus we retain all clouds with sizes larger than this.

Of greater concern are the possible effects of mass diffusion, since the standard Laplacian diffusive operator used in the continuity equation causes diffusion to be important over a larger range of scales than the hyperviscosity. Indeed, the characteristic diffusion time τ_{dif} can be shorter than the turbulent crossing time τ_{NL} for clouds smaller than about 16 pixels (see Appendix), and diffusion may dominate over turbulent advection for those clouds. In particular, it is

possible that the small, low-density clouds reported in the previous section might be a numerical artifact of the diffusion, which tends to reduce density peaks and spread the clouds out, or, conversely, to prevent clouds from reaching higher densities and smaller sizes than they do in the simulations.

Note, however, that the effect of mass diffusion is exclusively to damp density gradients originated by the turbulent velocity field, and so diffusion is incapable of forming clouds by itself; instead, it only modifies the properties of clouds formed by turbulence or other processes (gravity or the various instabilities discussed in Paper I). We can thus obtain a crude estimate of the size and maximum density a cloud would have in the absence of diffusion by integrating the diffusion equation backwards in time for initial conditions corresponding to the clouds in the simulation, over the length of a nonlinear time τ_{NL}. This correction overestimates the effects of diffusion, since it neglects the advection term entirely, and the nonlinear time is computed using the turbulent velocity associated to the size of the cloud, as given by the turbulent spectrum in fig. 10. However, it is actually turbulent scales larger than a cloud's size which are most likely to form it (Elmegreen 1993; Vázquez-Semadeni, Passot & Pouquet 1995b). In particular, in the simulations at least, clouds often form at the interfaces of expanding shells from previous star formation events, which may have velocities of several kilometers per second, rather than the significantly smaller velocities ($\lesssim 1$ km s^{-1}) indicated by the spectrum, which is a globally averaged quantity. Nevertheless, for robustness, we will use the worst-case correction. The details of this calculation are given in the Appendix. There it is shown that the central density of a cloud varies by factors of 3–5 in the worst cases under the influence of diffusion. Using this "correction" factor and assuming the clouds move along lines of constant mass in the density-size plot, one can produce a "corrected" such diagram, shown in fig. 16 in the Appendix for Run 28bis. There it can be seen that, although clouds are indeed brought slightly closer to a correlation, at the lowest average densities cloud sizes still vary by factors of about 100, maintaining the conclusions from §3.

As a further test, we have also produced a preliminary higher-resolution run, labeled Run 28.800, similar to Run 28bis, but at a resolution of 800×800 pixels, the largest that we can perform in the CRAY YMP of DGSCA, UNAM. The density field for this run is shown in fig. 7. In order to produce this run, the data from Run 28 at $t = 6.5 \times 10^7$ yr were interpolated to produce initial conditions for the 800×800 simulation, and then evolved for another 0.65×10^7 yr, enough to develop the additional small scale structure corresponding to the larger resolution. Incidentally, it is worth noting that, even though Run 28.800 has a resolution only $\sim 60\%$ larger than Runs 28 and 28bis, the computational effort it requires is roughly 5 times larger in CPU run time. Fig. 8 shows the resulting density-size raw plot for this run, including cloud sizes down to 1 pixel. In the Appendix, fig. 17 shows the corresponding plot incorporating the corrections described above, namely elimination of clouds with sizes ≤ 4 pixels, and the correction for diffusion. In order to maximize the available dynamic range, in the figures in the Appendix we have used values of the density threshold as low as $\rho_{\mathrm{t}} = 0.5$. For Run 28.800, it is seen that the clouds with the lowest average densities span a range of roughly a factor of 200 in sizes after the corrections, while the raw data exhibit a range of a factor ~ 500.

In summary, the discussions from this section suggest that the existence of small clouds with low densities described in §3 is a true consequence of the dynamics and not an artifact of the dissipative terms used to stabilize the equations.

4.2. Implications of the results

4.2.1. Density, size and equilibrium

With the above considerations in mind, we then have a number of direct implications. First, as already stated above, the absence of a density-size relation implies non-constant column densities for the clouds. Specifically, cloud column densities vary by over two orders of magnitude in the simulations. Additionally, the result that clouds with sizes down to the smallest scales exist at all values of the mean density implies that the observed density-size relation may indeed be a product of the limited dynamic range of typical surveys. Under these conditions, the derived column densities could appear to show variation over a modest range only, while the observed sizes might span a range larger than three orders of magnitude, thus creating an apparent correlation. Observational effects as a possible origin of the density-size relation were first suggested by Larson (1981) himself, and later discussed in more detail by Scalo (1990). Another reason for the appearance of a spurious density-size

relation may be a selection effect introduced by the tendency of observational work to focus primarily on global intensity maxima of the maps, therefore possibly missing weaker, local maxima, a bias that only recently has started to be avoided (e.g., FPP).

The Larson-type relation defined by the largest clouds, with a scaling exponent $\alpha \sim -0.8 \pm .16$ is particularly interesting. The immediate question that arises is whether this relation is physical, or is induced by numerical constraints. On the physical side, a first consideration is that, if the clouds are hierarchically nested (smaller, denser clouds are part of larger, less-dense ones), then mass conservation implies $-\alpha < 3$ in three dimensions. In our two-dimensional case, this limit becomes $-\alpha < 2$. This is a physical limit which in the simulations is pushed closer to the observed relation because of the two-dimensionality.

Another physical issue is whether the large clouds which follow a density-size scaling law are virialized, so that the standard scenario in which Larson's relations hold for virialized clouds would apply to the largest clouds. However, examining cloud virialization in our simulations turns out not to be a straightforward task(§4.2.2). Here, we just check whether the standard Δv-R relation is also satisfied in the large clouds. To this end, some clouds in figs. 4 and 5 have been labeled with numbers so that they can be identified from one figure to another. Interestingly, for Run 28 at $t = 6.6 \times 10^7$ yr (case a in the figures), the largest clouds, which are very close to the constant-column density line $\rho \sim R^{-1}$, shown as the straight line in fig. 5a, are also very close to the line $\Delta v \sim R^{1/2}$ in fig. 4a, suggesting balance between gravity and turbulence for this set of clouds. However, this is not the case for the clouds in Run 28bis at $t = 7.15 \times 10^7$ yr (case b in the figures). In this case, although the clouds again show a slope very close to -1 (fig. 5b), it can be seen from fig. 4b that they all have comparable velocity dispersions. We conclude that even clouds with a $\rho \propto R^{-1}$ density dependence are not necessarily in equilibrium between turbulence and self-gravity. Possibly, magnetic support is more important for the latter set of clouds, as in the results of Myers & Goodman (1988).

An interesting question is whether the various clouds along the large column density "envelope" of the distribution in the density-size relation are essentially the same cloud seen at various different thresholds ρ_t, or else they are truly different clouds. In fact, the answer is that they are neither. This is exemplified in fig. 9, which shows a few selected branches of the cloud hierarchy for Run 28bis. One branch off the largest cloud includes all the clouds along the envelope, but both the largest and second largest clouds are seen to also have other branches to daughter clouds off the envelope (dotted lines). The same is true of clouds lying immediately below the envelope (dashed lines), which seem to define a second envelope of similar slope (see fig. 5).

On the numerical side, the mass diffusion term in the continuity equation may tend to reduce the column density of clouds defined through the threshold density-criterion we use here, since the diffusion widens and smooths clouds, whose outer parts may then be left out of the domain defined by ρ_t. This effect, plus the plain limitations imposed by the resolution, clearly prevent the formation of very small clouds with very large column densities, causing shallower slopes of the high-column density envelope. In fact, while the average slope we obtain implies smaller column densities for smaller clouds, it has been pointed out by Scalo (1985, sect. III.A) that it is obvious from inspection of Lynds' dark cloud catalog that smaller clouds are darker. Indeed, in our case, the correction discussed in 4.2.1 and in the Appendix tends to bring this envelope towards steeper slopes. In summary, the specific slopes defined by the largest clouds in the $\log \rho$–$\log R$ plot cannot be unambiguously attributed to real physical effects. High-resolution, three-dimensional simulations are needed to resolve this issue. Unfortunately, the largest simulations of supersonic compressible turbulence known to us (e.g., Porter, Pouquet, & Woodward 1994, using 512^3 grid points), are purely hydrodynamic and do not contain many essential ingredients of ISM dynamics, such as the magnetic field, self-gravity, and stellar (i.e., small-scale, compressible) forcing. Thus, the necessary calculations are still a few years in the future.

In any case, regardless of what the specific slope of the envelope turns out to be upon removal of numerical effects, our results suggest that the notion of a density-size scaling relation should probably be replaced by that of an "allowed" region in ρ–R space. Whether the high-column density boundary is truly a power law, the value of its corresponding index, and the physical mechanisms responsible for it, are issues that remain to be determined by high resolution 3D simulations.

4.2.2. Velocity dispersion-size relation and turbulence

Since the density-size relation is not verified for the clouds in the simulations, yet the dispersion-size relation is, the standard argument explaining the Δv–R relation, namely virial equilibrium in clouds satisfying $\rho \propto R^{-1}$, cannot be invoked. This implication is independent of the dimensionality of the simulations, as it only relies on the non-existence of a density-size relation, and not on particular values of the scaling exponents. That is, the two-dimensionality would, at most, change the exponent in the virial equilibrium relation between Δv and ρ, but not destroy the correlation altogether. Since in the simulations no density-size relation exists, a unique virial equilibrium relation between Δv and ρ does not exist either (although see § 4.2.3). Note, however, that a Jeans-type analysis incorporating a "turbulent pressure" (Chandrasekhar 1951; Scalo & Struck-Marcell 1984; Bonazzola et al. 1987; Elmegreen 1991; Vázquez-Semadeni & Gazol 1995) such that $\nabla P_{\mathrm{turb}} = (\Delta v)^2 \nabla \rho$ gives

$$\Delta v \sim R\rho^{1/2}, \tag{8}$$

for clouds of size R equal to their Jeans length. Since the latter is independent of dimensionality, relation (8) holds also independently of dimensionality. Thus, the same scaling laws as in 3D are expected for two-dimensional clouds in balance between self-gravity and turbulence. This is consistent with a crude estimate of virial balance in which one equates the gravitational energy W to the turbulent kinetic energy K. For simple cloud geometries and uniform densities and turbulent velocity dispersions, in 3D one obtains $GM^2/R \sim M(\Delta v)^2$. Taking $M \propto \rho R^3$ gives the usual result $(\Delta v)^2 \propto \rho R^2$. In 2D, on the other hand, $M \propto \rho R^2$, but the gravitational energy becomes $W \sim GM^2$, thus preserving the result $(\Delta v)^2 \propto \rho R^2$. However, such a simplified treatment may not be applicable, since in 2D logarithmic corrections appear, and also the gravitational term in the virial theorem may differ from the gravitational energy. A detailed analysis of this problem is in progress (Ballesteros-Paredes & Vázquez-Semadeni 1996). Thus, the instability analysis is provisionally a more reliable indicator of the equilibrium relation expected in 2D.

In the absence of a density-size relation, a plausible origin of the velocity dispersion-size relation is the statistical properties of the turbulence itself. Indeed, an index $\beta = 1/2$ is expected for turbulence characterized by an energy spectrum $E(k) \propto k^m$ with spectral index $m = -2$ (e.g., Bonazzola et al. 1987; Vázquez-Semadeni & Gazol 1995; Padoan 1995; Fleck 1996), where k is the wavenumber associated with scale $R = 2\pi/k$. Such a spectral index is the signature of a field of random shocks (see Passot, Pouquet & Woodward 1988 and references therein). Figure 10 shows the spectra for the incompressible (solid line) and irrotational (dashed line) parts of the velocity fields of fig. 1. For comparison, the straight dotted line shows a k^{-2} power law. It is clearly seen that the spectrum of the incompressible component is remarkably well described by this slope. The irrotational, or compressible, component exhibits somewhat stronger fluctuations (most likely due to the fact that the "stars" in the simulations inject purely compressible energy), but is still very close on the average. The 20% discrepancy with the index $\beta \sim 0.4$ found in the simulations may be due to the fact that in the simulations there exists an upper bound to the turbulent velocity dispersion (of order a few km s^{-1}) that can be imparted to the medium by the stellar heating, since in the model they only heat the gas to $\sim 10^4$ K. This introduces a "truncation" on the Δv-R relation, which flattens the resulting slope, as can be seen in figs. 4a and 4b.

4.2.3. An alternative interpretation

At this point, one important alternative must be pointed out. The large scatter in the velocity dispersion-size relation would be consistent with the clouds *not* having constant column densities, even if they were in equilibrium between turbulence and self-gravity. Indeed, in equilibrium, the scatter of about one order of magnitude in the velocity dispersion would imply a scatter of roughly two orders of magnitude in the column density, as can be seen from the equilibrium relation

$$\Delta v \sim (NR)^{1/2}, \tag{9}$$

which is equivalent to relation (8). Thus, our results can also be interpreted in the sense that all clouds tend to be virialized, although with a scatter of at least two orders of magnitude in the column density. Preliminary results on the energy budget of a smaller cloud sample in Run 28 (Ballesteros-Paredes & Vázquez-Semadeni 1995) suggest that the sum of the kinetic and magnetic energies is within one order of magnitude of the gravitational energy, although surface terms were not considered there. Also, the total gravitational and the turbulent kinetic energies

per unit mass in the simulations are almost in equipartition, as shown in fig. 11

In this alternative interpretation, a density-size correlation may still be present, but missed by the simulations because the scatter is larger than the column density dynamic range in the simulations (and in most observational studies). This scenario would leave the origin of the putative density-size relation unexplained, although it may still be possible that the Δv-R relation is originated by the turbulent energy spectrum, and that the ρ-R relation is the consequence of virial equilibrium. Although this scenario cannot be ruled out with certainty until significantly higher-resolution simulations are performed, it seems unlikely, because in the simulations, clouds with sizes down to the smallest resolved scale are often found even at the lowest values of ρ_t, thus not giving any indication of the presence of a density-size relation. Instead, clouds of similar average densities often span the whole range of scales accessible to them. Also, the global balance between the turbulent and gravitational energies is mostly just a consequence of the presence of a self-regulated cycle of gravitational contraction, star formation, energy injection to the medium and dispersal, and again gravitational contraction, as discussed in Vázquez-Semadeni et al. (1995a), so that near global balance between turbulence and self-gravity is maintained at all times.

Finally, note that here we have not discussed other mechanisms that have been suggested in the literature as responsible for the Δv-R relation, such as inverse cascades of angular momentum, (Henriksen & Turner 1984), critical thermal pressure equilibria (Chièze 1987) or the contribution from the magnetic support (Shu 1987; Myers & Goodman 1988; Mouschovias & Psaltis 1995; Gammie & Ostriker 1995). We will address the role of these processes in the simulations in future work.

4.3. Comparison with observations

The lack of correlation between cloud density and size in the simulations appears to be in contradiction with the correlations found in most observational results (Larson 1981; Torrelles et al. 1983; Dame et al. 1986; Falgarone & Pérault 1987; Myers 1990; WMD). However, as discussed in § 4.2.1, we interpret the discrepancy as an effect of the limited column density dynamic range of the observations or of selection effects introduced by focusing exclusively on global intensity maxima in the maps. There are some exam-

ples of observations that have intended to avoid these problems (Carr 1987; Loren 1989; FPP). The first two authors have focused on clumps within a single molecular cloud with extensive star formation, thus better sampling the non-gravitationally-bound turbulent transients. The work of FPP was specifically tailored towards studying low-brightness regions in molecular clouds. In both Loren (1989) and FPP, column densities spanning over one and a half orders of magnitude are found.

On the other hand, WMD have recently concluded from an analysis of 60 μm and 100 μm IRAS maps, that column densities of dark clouds cluster typically at $N(H_2) \simeq 4 \times 10^{21}$ cm^{-2} (corresponding to a typical 100 μm opacity of $\tau_{100} \simeq 200$ μNepers), while claiming that the dynamic range of the data would have allowed detection of any significant variations. The discrepancy between these results and those of the present paper seemingly cannot be explained in terms of the limited column density dynamic range of their observations.

In actuality, we believe that the results of WMD may be spurious and attributed to a combination of their selection criteria and the following effect. At 60 μm and 100 μm, one is observing "warm" dust that could be coming from the "edges" of molecular clouds. If this "warm" dust is being heated by the visible photons from the galactic stellar radiation field, it is expected that the depth of the "warm" region will be of order of a few Nepers in the visible. This will lead to apparent constant optical depths when determined from observations of the "warm" dust.

Detailed radiative transfer models have been presented by Bernard et al. (1992), whom have already warned against using 100 μm surface brightness as a tracer of dust column density. In what follows, we present a simpler model that allows us to give first-order estimates of the scaling of the intensities in the IRAS 60 and 100 μm bands and the *apparent* dust opacity as a function of the true dust opacity through the cloud.

Similarly to Jarrett et al. (1989) and WMD, we assume that the ratio of visible to 100 μm absorption efficiency is $(Q_V/Q_{100}) = 2.0 \times 10^4$. It is important to emphasize that the 100 μm opacity considered in this ratio is being produced by small dust particles that become heated to relatively large temperatures and that are responsible for the observed 100- and 60 μm emission. The absorption efficiency ratio that includes all the dust at 100 μm is about a

factor of 10 smaller (Chini, Krugel & Kreysa 1986). Furthermore, in the range of wavelengths between 60 and 100 μm, the absorption efficiency scales approximately as ν^{-1}. Using this functional dependence, we can write a crude approximation for the dust temperature as

$$T_{\mathrm{DUST}} = (T_{\mathrm{cr}}^5 + T_{\mathrm{RAD}}^5 \; e^{-\tau_{\mathrm{V}}})^{1/5},$$

where T_{cr} and T_{RAD} are pseudotemperatures that parameterize the heatings due to cosmic rays and radiation, respectively. (Although this approximation is not valid at all wavelengths, we have checked that using slightly different functional dependences does not significantly alter our results.) We assume that cosmic ray heating is constant for any point in the cloud. Specifically, $T_{\mathrm{cr}} = 10$ K is the temperature that the dust has if heated only by cosmic rays, and T_{RAD} is the temperature that the dust would have if heated only by the stellar radiation field (at the edge of the cloud, where no absorption is present). Also, τ_{V} is the opacity in the visible, that increases as we get deeper into the cloud. In this simple model $T_{\mathrm{DUST}} \simeq T_{\mathrm{RAD}}$ at the edge of the cloud and it tends to T_{cr} for the inner regions of the cloud (fig. 12). The intensities at 60 μm and 100 μm, I_{60} and I_{100}, can be calculated for clouds with different values of τ_{V}, as shown in fig. 13. This calculation is made assuming that $Q_{100}/Q_{60} = 60\mu/100\mu$. From this figure it is evident that for clouds exceeding a few Nepers in τ_{V}, I_{60} and I_{100} do not continue growing with τ_{V}. An apparent dust temperature, $T_{60/100}$ can be derived from I_{60} and I_{100} and the far-infrared opacities are then obtained. In fig. 14, we plot the 100 μm opacity derived in this manner as a function of the cloud's τ_{V} for different values of T_{rad}. The apparent 100 μm opacity "saturates" at values in the order of 70 to 100 μNepers. Considering that along a line of sight one expects to intersect the front and the back edges of a cloud, the typical 100 μm opacities of $\tau_{100} \simeq 200\mu$Nepers appear to be explained as a result of this effect. The few clouds with much larger values of τ_{100} (up to $\tau_{100} \sim 10^4$) reported by WMD are regions of strong star formation activity, which may heat the clouds from the inside, raising τ_{100}. The presence of this effect is also consistent with the limb brightening observed in some clouds in the far-infrared by Snell, Heyer & Schloerb (1989) and WMD, and predicted by the models of Bernard et al. (1992). Note that this effect continues to be applicable even if the clouds are clumpy, since it should hold at the edges of any

density peaks, large or small, as long as they have a large enough column density. However, note also that this "saturation" effect in the determination of the apparent τ_{100} will occur only if reasonably high temperatures ($T_{\mathrm{DUST}} \gtrsim 20$ K) are present at the cloud's surface. In any case, for lower dust temperatures the emission at 60 and 100 μm is very weak and undetectable in practice. One consequence of this effect is that in order to fully sample the dust from dark clouds one requires observations at longer wavelengths that will trace the predominant cooler dust component. We intend to verify this effect by comparing column densities obtained with different indicators in future work.

The effect discussed above may clearly impose an upper bound to the column densities derived by WMD. Furthermore, concerning their selection criteria, it should be noticed that WMD define core, cloud and cloud complex in terms of ranges of extinction. This directly selects against identification of low-column density structures. In fact, in their maps, small, low-extinction clouds are readily seen, but not classified as such precisely because of their low extinctions. Thus, the column densities of the cores studied by WMD are bound from above due to the "saturation" effect of the cloud edges, and from below by their very definition of a core, rendering their derived column density constancy open to question.

5. Summary and Conclusions

In this paper we have searched for Larson-type (1981) correlations and cloud mass spectrum slopes in the clouds generated in numerical simulations of the ISM, one from Paper I, a similar one with a larger density dynamic range, and another with higher resolution. We define a cloud as a connected set of pixels in the density field with values larger than an arbitrary threshold ρ_{t}. From the results at various different times in the two simulations, we find that the mass spectrum has the form $dN/dM \propto M^{-1.44\pm.1}$, and the velocity dispersion is related to the cloud size by $\Delta v \propto R^{0.41\pm.08}$, where the errors are the standard deviations in the set of values including all the various times. The dispersion-size relation exhibits a scatter of about an order of magnitude, comparable to the scatter observed in real clouds.

The simulated clouds do not exhibit a density-size relation, but instead, at all mean densities, clouds of sizes down to the smallest resolved scales are com-

10

monly found. This result implies that the clouds do not have constant column densities, but instead exhibit a range of roughly two orders of magnitude, thus providing strong support to the possibility that the observationally-derived density-size relation is an artifact of the limited dynamic range employed by observational surveys, and of the criteria used for selecting the clouds, as first noticed by Larson (1981), and then strongly argued for by Scalo (1990). Our results suggest that low-column density clouds do exist in the ISM, but are systematically missed by most observations. In the simulations, low-column density clouds are turbulent transients, as in the suggestion by Magnani et al. (1993). Observational work that has used complete cloud samples (e.g., Loren 1989), or specifically looked at structures in the low brightness regions of molecular clouds (FPP), has indeed found a reported column density variability of over one and a half orders of magnitude, and masses well below the virial mass, by factors up to two orders of magnitude. However, note that in our simulations most of the mass resides in the largest clouds at each mean density, since there are comparable numbers of small and large clouds.

The set of largest clouds at every threshold ρ_t exhibits a density-size relation $\rho \sim R^\alpha$, with $\alpha = -0.8 \pm .15$. These clouds appear to be close to balance between turbulence and self-gravity on occasions, but not in general. On the other hand, pure mass conservation, which gives an upper limit $-\alpha < 2$ for the two-dimensional case, together with numerical limitations of the simulations, cannot be ruled out as the sole causes responsible for this result. In any case, regardless of what the specific slope of the envelope turns out to be upon removal of numerical effects, our results suggest that the notion of a density-size scaling relation should probably be replaced by that of an "allowed" region in ρ–R space. Whether the high-column density boundary is truly a power law, the value of its corresponding index, and the physical mechanism responsible for it, are issues that remain to be determined by high resolution 3D simulations.

The result that the Δv-R relation is verified in the simulations but the ρ-R relation is not, supports the interpretation that the former relation is a direct consequence of the statistical properties of the turbulence, since a turbulent energy spectrum of the form $E(k) \sim k^{-2}$, as observed in the simulations, implies an $R^{1/2}$ scaling for the velocity dispersion. However, we discussed the possibility that a density-size rela-

tion does exist, although with a scatter larger than the column density dynamic range spanned by the clouds in the simulations. Such a scatter would be consistent with balance between turbulence and self-gravity, with a scatter of one order of magnitude in the velocity dispersion, according to relation (9). In this case, the origin of the ρ-R relation would remain unknown, and the turbulent origin of the Δv-R relation would have not as strong a support. This possibility cannot be ruled out without very high resolution simulations in order to add at least another order of magnitude to the column density dynamic range. However, the simulations do not give any indication that this may be the case, since cloud sizes down to the smallest resolved scales are found even at the lowest values of ρ_t. Besides, the column density dynamic range in the simulations is already larger than that of most observational surveys.

We also discussed the recent results of WMD, who have argued in favor of a surprisingly constant column density (to within a factor of a few) in a large sample of cores studied through IRAS 60 and 100 μm maps, while claiming a very large dynamic range in their observational method. We argued that this result may be spurious, by presenting a model in which the warm "skin" of clouds and cores, which is likely to always have visual extinctions of order unity, puts an upper bound to the column densities measured by WMD. From below, WMD's own selection criteria eliminate low-column density clouds, thus mimicking a nearly uniform column density.

Finally, we remark that in this paper we have limited the discussion to the trends of the density and velocity dispersion with size, omitting any discussion of the role of the magnetic field, which is clearly important for the dynamics of the simulations (Paper I). A detailed account of the energy budget in the simulations including the magnetic energy density, as well as surface terms is under way (Ballesteros-Paredes & Vázquez-Semadeni 1996).

6. APPENDIX

In this appendix we make an order of magnitude estimate of the effect of the numerical difussion term in the continuity equation. Consider the continuity equation, eq. (3):

$$\frac{\partial \rho}{\partial t} + \nabla \cdot (\rho \mathbf{u}) = \mu \nabla^2 \rho. \qquad (10)$$

In order to estimate the effects of difussion, we consider the extreme case when the advection term can be neglected, so that the mass equation becomes the standard difussion equation:

$$\frac{\partial \rho}{\partial t} = \mu \nabla^2 \rho. \qquad (11)$$

For simplicity, we consider a one-dimensional (axisymmetric) problem, whose solution is (see, e.g., Habbermann 1987):

$$\rho(x,t) = \sqrt{\frac{1}{4\pi\mu t}} \int_{-\infty}^{+\infty} f(x') \exp\left(-\frac{(x-x')^2}{4\mu t} \right) dx', \qquad (12)$$

where $f(x')$ is the initial density distribution, which we assume to be a Gaussian, $f(x') = \rho_0 \exp(-x'^2/2\sigma^2)$. In what follows, we will identify the width σ of the Gaussian with the size of the cloud of interest. Equation (12) then becomes:

$$\rho(x,t) = \rho_0 \left(\frac{1}{t/t_0 + 1} \right)^{1/2} \exp\left(-\frac{x^2/2\sigma^2}{t/t_0 + 1} \right), \quad (13)$$

where

$$\left(\frac{t_0}{t_{\text{code}}} \right) = \frac{\sigma^2}{2\mu} = 9.41 \times 10^{-3} \left(\frac{\sigma}{\text{pixels}} \right)^2. \qquad (14)$$

is the characteristic diffusion time in units of the code, $t_{\text{code}} = 1.3 \times 10^7$ yr, and the second equality follows from using the value $\mu = 0.008$ (see Paper I) (note that the size of the integration box is 2π in the code units). This value of t_0 can be made independent of the resolution of the simulation by choosing μ such that $\mu k_{\max}^2 = \text{cst}$, where $k_{\max}$ is the maximum Fourier wave number in the simulation, equal to $1/2$ of the resolution.

Now consider the turbulent crossing (or nonlinear) time for scale σ:

$$\tau_{\text{NL}} \sim \sigma/u_l,$$

where u_l is the turbulent speed associated to the scale l. Note that we are allowing for the possibility that clouds of size σ are generated by turbulent streams of different, typically larger, size l (see §4.1). This velocity can be estimated from the turbulent energy spectrum $E(k)$ as:

$$\frac{1}{2} u_l^2 = \int_{2\pi/l}^{\infty} E(k) \, dk,$$

that is, u_l is the root mean square energy per unit mass in scales smaller than l. Using $E(k) = 0.1k^{-2}$, as indicated by fig. 10, one obtains:

$$\left(\frac{\tau_{\text{NL}}}{t_{\text{code}}} \right) = 14.05 \left(\frac{l/\text{pixels}}{n_{\text{res}}/\text{pixels}} \right)^{1/2}, \qquad (15)$$

where n_{res} is the number of pixels (i.e., the resolution) per spatial dimension of the simulation. From equations (14) and (15), we can now compare the diffusion and nonlinear times, in order to determine the scale at which they are equal. Assuming that $l = m\sigma$, we obtain:

$$\left(\frac{l_{\text{eq}}}{\text{pixels}} \right) = \frac{16.33}{m^{1/2}}, \qquad (16)$$

and thus, clouds with sizes lower than ~ 16 pixels are dominated by the numerical mass-difussion. Therefore, it is important to assess the effect of mass diffusion in the results of §3. To do this, we take the extreme position that for time durations $\Delta t \leq \tau_{\text{NL}}$, a Gaussian cloud is affected exclusively by diffusion, and compute the fractional variation of its central density over τ_{NL}. In fig. 15 we show the evolution of $\rho(0,t)/\rho_0$ given by equation (13) over τ_{NL} for a cloud of size $\sigma = 4$ pixels. Note that this is a worst-case estimate, since on the one hand, in the plots below we have discarded clouds with sizes ≤ 4 pixels in order to avoid viscosity effects (see §4.1), which is most affected by diffusion, while, on the other hand, we have taken $m = 1$.

As we can see from fig. 15, the density decreases by a factor $\lesssim 5$. Typically, thus, we can expect our density data to change by factors smaller than half an order of magnitude.

Using the above results, we can produce a "corrected" density-size plot with the estimated "true"

densities ρ_{corr} calculated as:

$$\rho_{\mathrm{corr}} \sim \rho_{\mathrm{data}}(1 + \tau_{\mathrm{NL}}/t_0)^{1/2}. \qquad (17)$$

where ρ_{data} are the raw cloud mean densities as produced by the simulations, and the "true" sizes are obtained assuming mass conservation:

$$R_{\mathrm{corr}} \sim \frac{R_{\mathrm{data}}}{(1 + \tau_{\mathrm{NL}}/t_0)^{1/4}}. \qquad (18)$$

The "corrected" density-size plots are shown in figs. 16 and 17 for Run 28bis and the high-resolution Run 28.800, respectively. We see that, although slightly pushed closer to a correlation in the case of Run 28 bis, the general trend of these plots still supports the main conclusion from §3, namely that clouds of sizes down to the resolution are seen at all mean densities.

REFERENCES

Babiano, A., Basdevant, C., Legras, B., & Sadourny, R. 1987, J. Fluid Mech., 183, 379

Ballesteros-Paredes, J. & Vázquez-Semadeni, E., 1995, in Fifth Mex-Tex Meeting in Astrophysics. Gaseous Nebulae and Star Formation, ed. M. Peña, & S. Kurtz, Rev. Mex. Astron. Astrof. Ser. Conf. 3, 105

Ballesteros-Paredes, J. & Vázquez-Semadeni, E., 1996, in preparation

Bernard, J. P., Boulanger, F., Desert, F. X., & Puget, J. L. 1992, A&A, 263, 258

Blitz, L. 1991, in The Physics of Star Formation and Early Stellar Evolution, ed. C. J. Lada, N. D. Kylafis (Dordrecht: Kluwer), 3

Blitz, L. 1994, in The Cold Universe, ed. T. Montmerle, C. J. Lada, I. F. Mirabel, & J. Trân Thanh Vân (Gif-sur-Yvette: Editions Frontières), 99

Bonazzola, S., Falgarone, E., Heyvaerts, J., Pérault, M., & Puget, J. L. 1987, A&A, 172, 293

Carr, J. S. 1987, ApJ, 323, 170

Caselli, P. & Myers, P. C. 1995, ApJ, 446, 665

Chandrasekhar, S. 1951, Proc. R. Soc. London, 210, 26

Chièze, J. P. 1987, A&A, 171, 225

Chini, R., Krugel, E., & Kreysa, E. 1986, A&A, 167, 315

Dame, T., Elmegreen, B. G., Cohen, R., Thaddeus, P. 1986, ApJ, 305, 892

Dickman, R. L., Snell, R. L., & Schloerb, F. P. 1986, ApJ, 309,326

Elmegreen, B. G. 1991, ApJ, 378, 139

Elmegreen, B. G. 1993, ApJ (Lett.), 419, L29

Falgarone, E., & Pérault, M. 1987, in Physical Processes in Interstellar Clouds, ed. G. Morfill, & M. Scholer (dordrecht: Reidel), 59

Falgarone, E., Phillips, T. G., & Walker, C. K. 1991, ApJ, 378, 186

Falgarone, E., Puget, J.-L., & Pérault, M. 1992, A&A, 257, 715 (FPP)

Fleck, R. C. 1996, ApJ, 458, 739

Fuller, G. A., & Myers, P. C. 1992, ApJ, 384, 523

Gammie, C. & Ostriker, E. 1996, preprint

Habbermann, R. 1987, Elementary Applied Partial Differential Equations with Fourier Series and Boundary Value Problems (New Jersey: Prentice Hall)

Henriksen, R., & Turner, B. 1984, ApJ, 287, 200

Jarrett, T. H., Dickman, R. L., & Herbst, W. 1989, ApJ, 345, 881

Larson, R. B. 1981, MNRAS, 194, 809

Loren, R. B. 1989, ApJ, 338, 902

Magnani, L., LaRosa, T. N., & Shore, S. N. 1993, ApJ 402, 226

Massi, M. & Lizano, S. 1994, A&A, 287, 581

McWilliams, J. 1984, J. Fluid Mech., 146, 21

Miesch, M. S., & Bally, J. 1994, ApJ, 429, 645

Mouschovias, , T. C., & Psaltis, D. 1995, ApJ, 444, L105

Mundy, L. G. 1994, in Clouds, Cores, and Low Mass Stars, ed. D. P. Clemens, & R. Barvainis (San Francisco: ASP), 35

Myers, P. C. 1990, in Molecular Astrophysics, ed. T. W. Hartquist (Cambridge: University Press), 328

Myers, P. C., & Goodman, A. A. 1988, ApJ, 326, L27

Padoan, P. 1995, MNRAS, in press

Passot, T., Vázquez-Semadeni, E., & Pouquet, A. 1995, ApJ, in press (Paper I)

Passot, T., & Pouquet, A., J. Comp. Phys. 75, 300

Passot, T., Pouquet, A. & Woodward P., 1988, A&A, 197, 228.

Porter, D. H., Pouquet, A., & Woodward, P. R. 1994, Phys. Fluids, 6, 2133

Scalo, J. M., & Struck-Marcell, C. 1984, ApJ, 276, 60

Scalo, J. M. 1985, in Protostars and Planets II, ed. D. C. Black & M. S. Matthews (Tucson: Univ. of Arizona Press), 201

Scalo, J. M. 1987, in Interstellar Processes, ed. D. J. Hollenbach & H. A. Thronson (Dordrecht: Reidel), 349

Scalo, J. M. 1990, in Physical Processes in Fragmentation and Star Formation, ed. R. Capuzzo-Dolcetta, C. Chiosi, & A. di Fazio (Dordrecht: Kluwer), 151

Shu, F. 1987, in Star Formation in Galaxies, ed. C. Persson (Washington: NASA Office of Space Science and Applications), 743

Snell, R. L., Heyer, M. H., & Schloerb, F. P. 1989, ApJ, 337, 738

Torrelles, J. M., Rodríguez, L. F., Cantó, J., Carral, P., Marcaide, J., Moran, J. M., & Ho, P. T. P. 1983, ApJ, 274, 214

Vázquez-Semadeni, E., & Gazol, A. 1995, A&A, 303, 204

Vázquez-Semadeni, E., Passot, T. & Pouquet, A. 1995a, ApJ, 441, 702

Vázquez-Semadeni, E., Passot, T., & Pouquet, A. 1995b, in Fifth Mex-Tex Meeting in Astrophysics. Gaseous Nebulae and Star Formation, ed. M. Peña, & S. Kurtz, Rev. Mex. Astron. Astrof. Ser. Conf. 3, 61

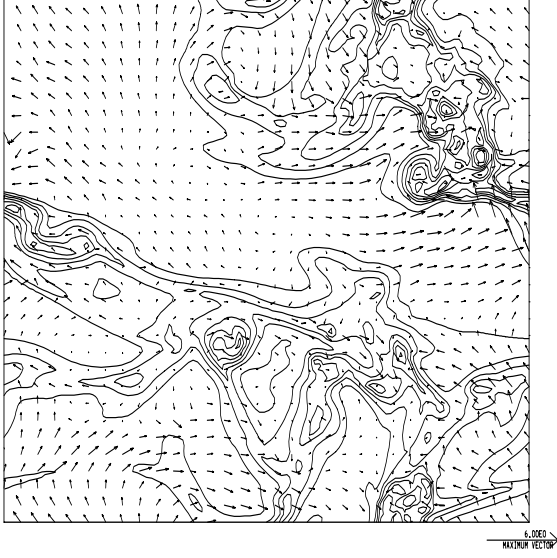Wood, D. O. S., Myers, P. C., & Daugherty, D. 1994, ApJS, 95, 457 (WMD)

Fig. 1.— Density (contours) and velocity (arrows) fields for Run 28 at $t = 6.6 \times 10^7$ yr. The contours are spaced logarithmically, with increments of 0.3125 in $\log \rho$. The minimum density in this plot is 0.04 cm^{-3}, and the maximum density is 40 cm^{-3}.
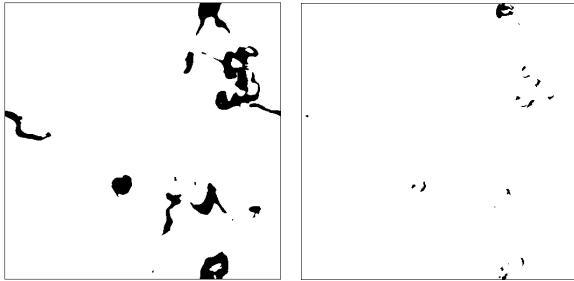

Fig. 2.— Regions ("clouds") with densities larger than an arbitrary threshold ρ_t in the density field of Run 28 at $t = 6.6 \times 10^7$ yr. a) $\rho_t = 4$. b) $\rho_t = 16$. Note that small clouds with high densities are nested within larger complexes, but small clouds with low densities can be seen in a) as well.
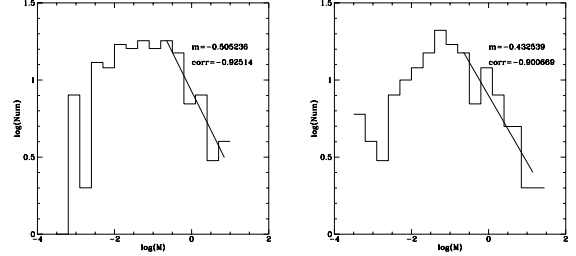

Fig. 3.— Logarithmic mass distributions for a) Run 28 at $t = 6.6 \times 10^7$ yr and b) Run 28bis at $t = 7.15 \times 10^7$ yr. The lines show least-squares fits to data bins with $\log M > 0.8$, and have slopes -0.51 in a) and -0.43 in b).
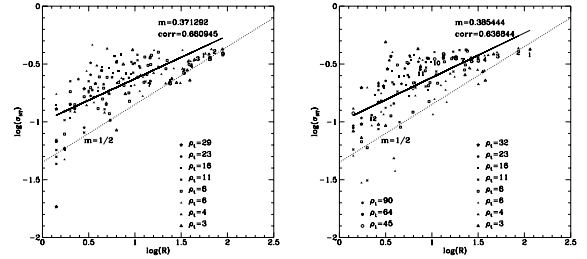

Fig. 4.— Velocity dispersion *vs.* size for all clouds in a) Run 28 at $t = 6.6 \times 10^7$ yr and b) Run 28bis at $t = 7.15 \times 10^7$ yr. Clouds obtained with each value of ρ_t are shown with a specific symbol as indicated. The solid lines show least-squares fits, with the slopes and correlation coefficients indicated. For reference, a 1/2 slope is indicated by the dotted lines. The cloud labels in a) and b) are respectively the same as in a) and b) of figs. 5a and b.
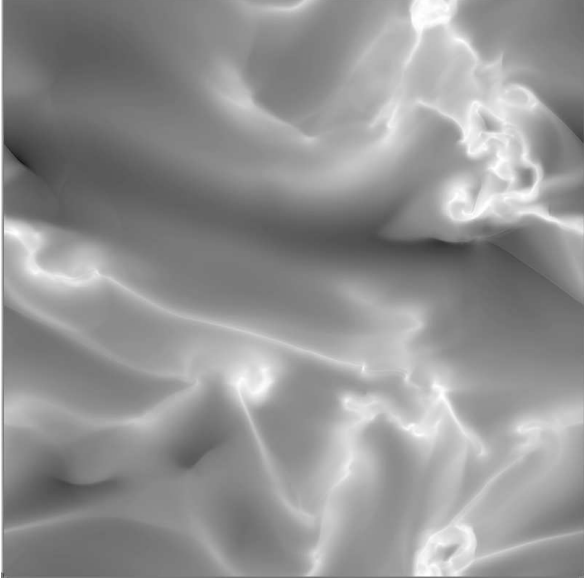
15

Fig. 5.— Average cloud density *vs.* size for for all clouds in a) Run 28 at $t = 6.6 \times 10^7$ yr and b) Run 28bis at $t = 7.15 \times 10^7$ yr. The lines show a $\rho \propto R^{-1}$ power law. In both cases, the largest cloud at each $\rho_{\rm t}$ lies near the $\rho \propto R^{-1}$ line, although other times tend to show shallower envelopes (see fig. 6). The full ensemble of clouds does not show any trend of $\langle \rho \rangle$ with R. The cloud labels in a) and b) are respectively the same as in a) and b) of figs. 4a and b.

Fig. 6.— Average density *vs.* size for the largest cloud at each value of $\rho_{\rm t}$ at six different times in Run 28 (bottom curves) and three times in Run 18bis (top curves, labeled "b"). Each point denotes the largest cloud at one value of $\rho_{\rm t}$. Different values of $\rho_{\rm t}$ for the same time in the simulation are joined by dotted lines and indicated with the same symbol. The various curves are displaced by increments of 0.2 in $\log \rho$ for clarity. The numbers next to each curve show the time into the evolution of the run to which it corresponds, in units of 10^7 yr. Note that time $t = 6.6 \times 10^7$ yr for Run 28 and time $t = 7.15 \times 10^7$ yr for Run 28bis have some of the steepest slopes. The straight line shows a $\rho \propto R^{-1}$ power law. The average slope for all times is -0.81, with a standard deviation of 0.16. Because of the "compression" at high densities due to various numerical effects, only clouds with $\log R > 1$ (Run 28bis) or $\log R > 1.5$ (Run 28bis) were considered in the calculation of the average slope (see text).

Fig. 7.— Logarithmic grayscale image of the density field of run 28.800 at time $t = 7.15 \times 10^7$ yr. This run is similar to run 28bis, except that it has larger resolution (800×800), and that star formation is turned off at time $t = 6.9 \times 10^7$ yr. The density extrema are $\rho_{\max} = 129$, and $\rho_{\min} = 3.4 \times 10^{-2}$.
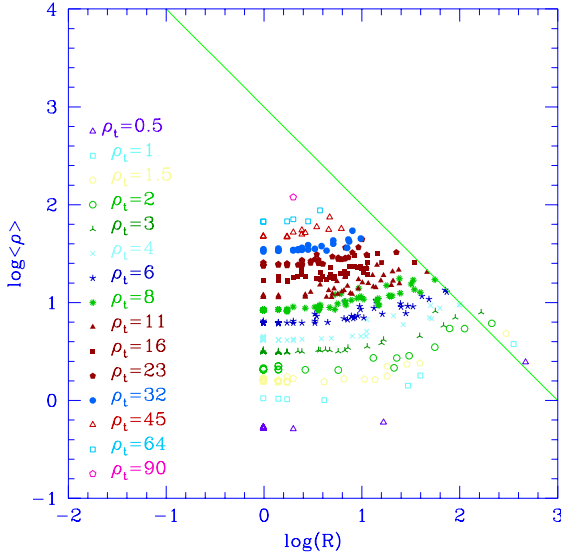

Fig. 8.— Mean density-size plot, equivalent to figs. 5a and b, but for the high-resolution Run 28.800. A large range of sizes, in this case spanning over two and a half orders of magnitude, is again seen at the lowest values of the average cloud density.
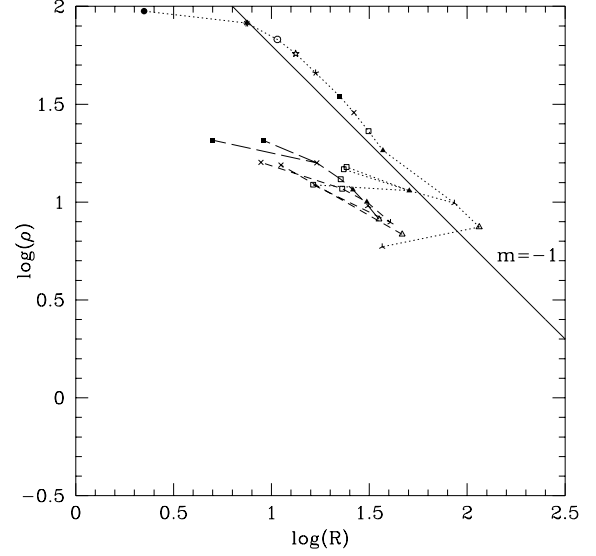
Fig. 9.— "Familiy tree" of a few selected clouds from fig. 5b. The largest cloud is seen to branch off to both clouds defining a Larson-type relation as well as to clouds away from it (dotted lines). A similar branching pattern is observed for clouds of lower column densities (dashed lines).
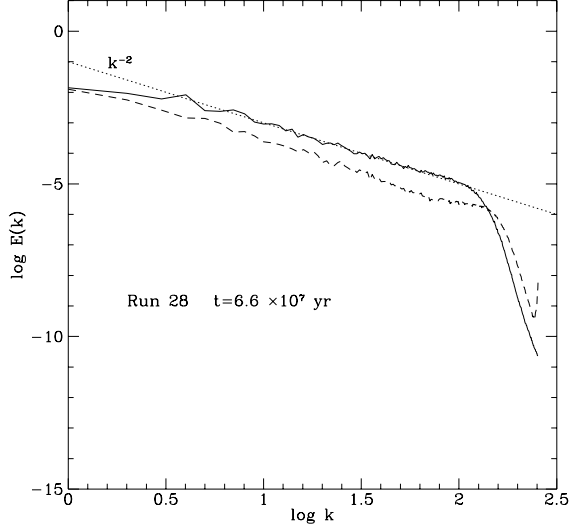
Fig. 10.— Turbulent energy spectra for Run 28 at $t = 6.6 \times 10^7$ yr. *Solid* line: incompressible component of the spectrum. *Dashed* line: compressible component. The straight line shows a k^{-2} power law, characteristic of shocks, which implies an $R^{-1/2}$ dependence of the velocity dispersion.
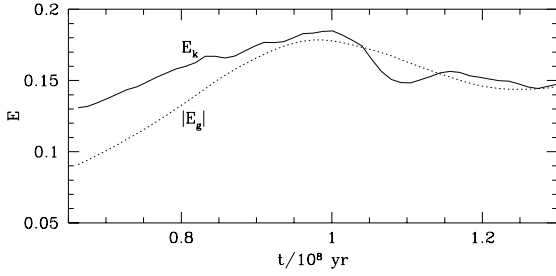

Fig. 11.— Evolution of the total turbulent kinetic (*solid line*) and the gravitational (*dotted line*) energies per unit mass in code units for run 28 over the last half of its evolution. The two energies are very close to equipartition at all times.
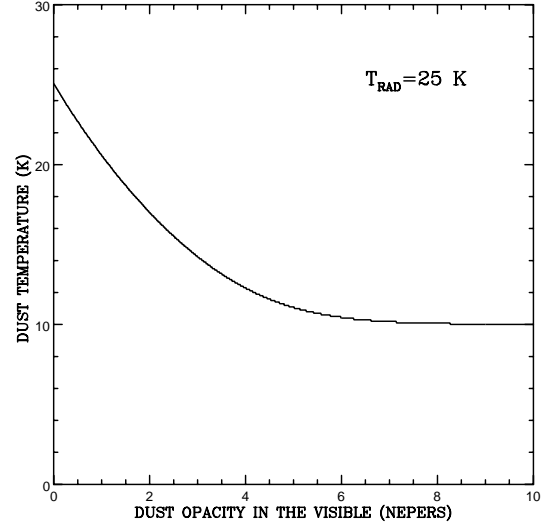
Fig. 12.— Dust temperature, T_{DUST}, as a function of dust opacity in the visible for $T_{RAD} = 25$ K. Near the edge of the cloud (left side) T_{DUST} tends to T_{RAD}, while toward the inner regions of the cloud (right side) heating by radiation becomes negligible and T_{DUST} tends to the value provided by cosmic ray heating (10 K in our model).
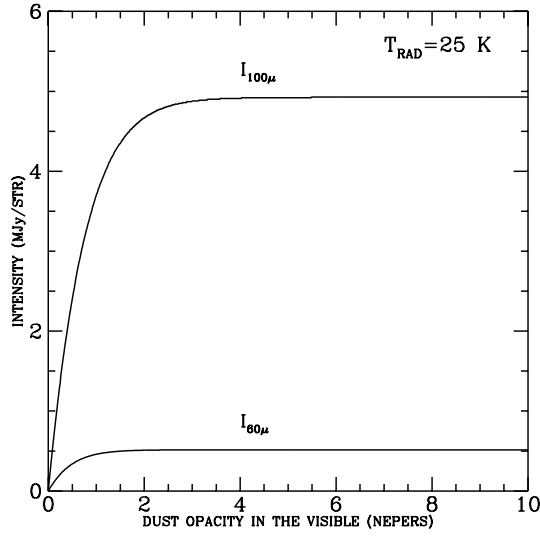
18

Fig. 13.— Intensity of cloud emission at 100 μm and 60 μm as a function of dust opacity in the visible, for T_{RAD}=25 K. Note that the growth of the intensity "saturates" above a few Nepers of dust opacity in the visible. The reason for this effect is that beyond a few Nepers of dust opacity in the visible there is no significant radiation heating and the dust becomes too cold to emit significantly at 100 μm and 60 μm.
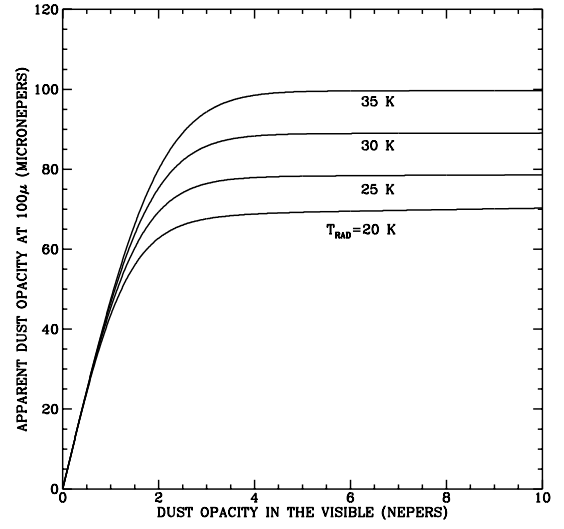

Fig. 14.— Apparent warm dust opacity at 100 μm (derived from the intensities at 100 μm and 60 μm), as a function of dust opacity in the visible for different values of T_{RAD}. Note the "constancy" in the apparent dust opacity at 100 μm once the cloud exceeds a few Nepers in dust opacity in the visible, practically independently of T_{RAD}.
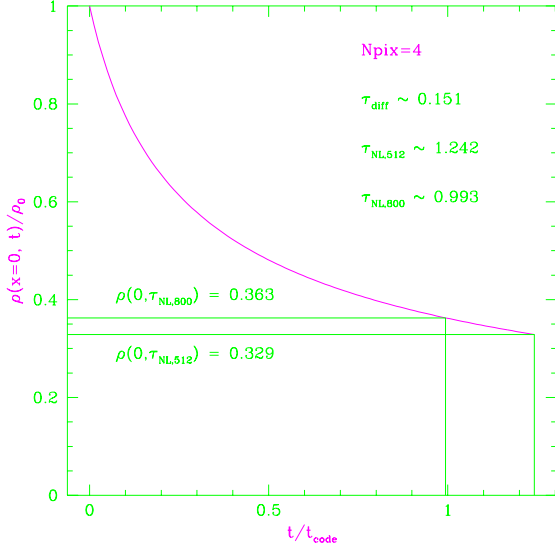
Fig. 15.— Fractional change of the central density $\rho(0,t)/\rho_0$ of a cloud of size 4 pixels. The fractional change shown here is an upper bound to the corrections applied to the simulated data, since we have considered a cloud with size smaller than the minimum cloud size retained, and $m = 1$ in eq. (16).
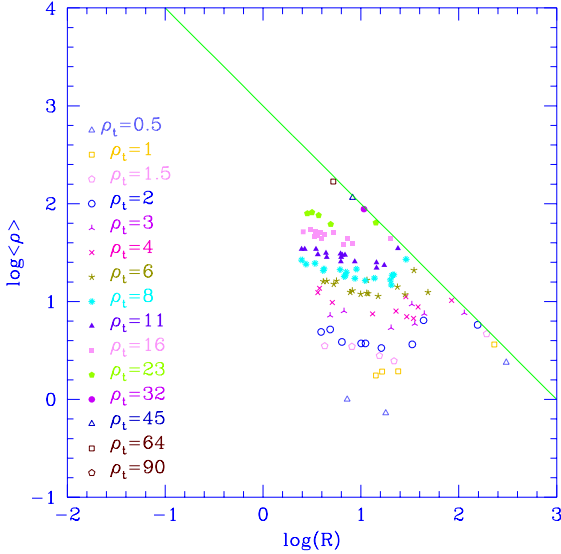

Fig. 16.— "Corrected" density-size plot for Run 28bis using the estimates for the 'true" density and size of the clouds given by equations (17) and (18). Note that a range of roughly two orders of magnitude in size remains for the lowest mean density clouds.
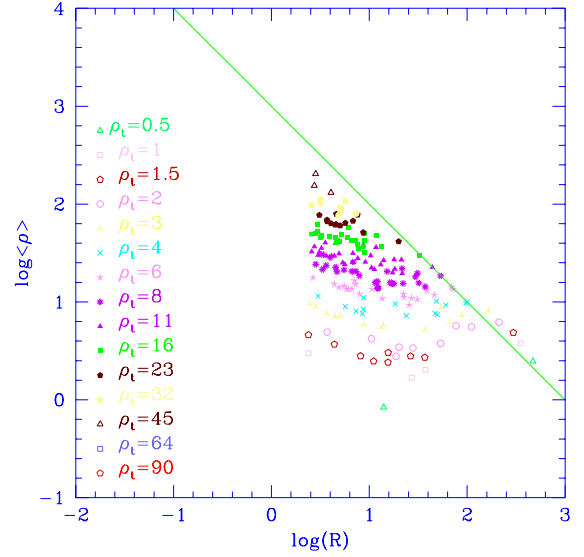

Fig. 17.— Same as figure 16, but for a Run 28.800. Here, the sizes of the smallest-density clouds vary by nearly 2.5 orders of magnitude. Note that, although only clouds with sizes larger than 4 pixels are retained, the smallest clouds in this figure have sizes smaller than that because of the size "correction", eq. (18).